Nanoscale Res Lett (2008) 3:249–254
DOI 10.1007/s11671-008-9144-2

NANO EXPRESS

Scanned Probe Oxidation on *p*-GaAs(100) Surface with an Atomic Force Microscopy

Sheng-Rui Jian · Jenh-Yih Juang

Received: 9 April 2008 / Accepted: 23 June 2008 / Published online: 3 July 2008

Abstract Locally anodic oxidation has been performed to fabricate the nanoscale oxide structures on *p*-GaAs(100) surface, by using an atomic force microscopy (AFM) with the conventional and carbon nanotube (CNT)-attached probes. The results can be utilized to fabricate the oxide nanodots under ambient conditions in noncontact mode. To investigate the conversion of GaAs to oxides, micro-Auger analysis was employed to analyze the chemical compositions. The growth kinetics and the associated mechanism of the oxide nanodots were studied under DC voltages. With the CNT-attached probe the initial growth rate of oxide nanodots is in the order of $\sim$300 nm/s, which is $\sim$15 times larger than that obtained by using the conventional one. The oxide nanodots cease to grow practically as the electric field strength is reduced to the threshold value of $\sim 2 \times 10^7$ V cm^{-1}. In addition, results indicate that the height of oxide nanodots is significantly enhanced with an AC voltage for both types of probes. The influence of the AC voltages on controlling the dynamics of the AFM-induced nanooxidation is discussed.

Keywords Atomic force microscopy · *p*-GaAs(100) · Nanooxidation · Multi-walled carbon nanotube · Auger electron spectroscopy

S.-R. Jian (✉)
Department of Materials Science and Engineering,
I-Shou University, Kaohsiung 840, Taiwan, ROC
e-mail: srjian@gmail.com

J.-Y. Juang
Department of Electrophysics, National Chiao Tung University,
Hsinchu 300, Taiwan, ROC

Introduction

Scanning probe microscopes (SPM) techniques have demonstrated potential in the creation and characterization of structures, patterns, and devices at the nanometer scale. In particular, atomic force microscopy (AFM) local anodic oxidation [1] is one of the most versatile methods for defining structures at the nanometer scale in the surface of anodizable materials. This technique has been applied to define a fairly large range of nanostructures [2] and nanodevices, like Josephson junctions, superconducting quantum interference devices (SQUID) [3], and single electron transistor (SET) devices [4–6].

Carbon nanotubes (CNTs) have been known to be ideal material for an AFM probe because of their cylindrical shape, small diameter, high aspect ratio, large Young's modulus [7], and unique chemical properties which reduce their physical and chemical changes during the scanning process [8]. In addition, CNTs have considerable mechanical flexibility and, therefore, can be elastically buckled without damage [9]. The application of CNT probes for nanooxidation [10] began almost simultaneously with the improvement in resolution for image measurements [11]. It is expected that the improvement of probe will open up the great possibilities for miniaturization, because the size of fabricated oxide nanostructures is predominantly determined by the probe apex. An effective way to decrease the probe apex is by means of CNT [12].

However, to successfully adopt the oxide nanodots and nanowires as integrated parts of the nanodevices, for instance, to serve as the effective tunnel barriers for carrier transport, further improvements/enhancements on the aspect ratio of oxide structures are needed. Herein, to optimize the condition of the anodic oxidation reaction under the probe, various conditions including the applied voltages, humidity,

the geometry of AFM tip, as well as the modulated voltages should be controlled. In this study, we compare the lithography results between two different types of AFM probes, the MWCNT probe and the conventional Si probe, used to fabricate the oxide nanostructures on *p*-GaAs(100) surface under ambient conditions. By identifying how the apex dimensions of the AFM probe influences the features of the resultant oxide nanostructures has lent us a key to further improve the aspect ratio of oxide nanostructures. The proper control of the oxidation reaction, improvement of reproducibility and increasing the accuracy are among the immediate objectives for further evolution of this technique.

Experimental Details

Nanolithography was carried out by using a commercial AFM (NT-MDT Solver-P47, Russia) in the noncontact mode (nc-AFM) at room temperature with the relative humidity of 55% in the present work. Two different types of AFM probes were employed: (1) a modified cantilever (Daiken-Kagaku, 3 N m^{-1}, 157 kHz) with a conductive MWCNT ($\sim$10 nm in diameter and $\sim$300 nm in length) attached on Si probe and (2) a conventional Pt-coated Si probe with the curvature radius of $\sim$35 nm, the force constant of 34 N m^{-1}, and the resonance frequency of 350 kHz, respectively. The sample was a *p*-GaAs(100) wafer with the resistivity of 10 Ω cm and root-mean-square surface roughness being less than 0.25 nm.

By applying a bias voltage between the *p*-GaAs(100) surface and the AFM probe, the oxide nanostructures were grown on the electrochemically reactive surface. For oxide nanodots anodization, the applied anodized voltage was at 8 V with the pulse duration ranging from 0.01 to 100 s. The anodization has been practiced over various surface positions through the AFM probe. For the voltage modulation studies, an AC voltage was applied to the AFM probe, where the amplitudes of the high- and low-level voltage were 8 V and −8 V, respectively, and both have the corresponding pulse durations of 50 ms. In the present work, the presented data are an average of five measurements.

To investigate the conversion mechanisms of GaAs-oxides, the chemical composition of the sample and some selected anodized regions was analyzed by Auger electron spectroscopy (AES, Auger 670 PHI Xi, Physical Electronics, USA) system equipped with a Schottky field emission electron source with the incident energy of 2 keV.

Results and Discussion

To optimize the AFM anodic oxidation process, it is necessary to understand the underlying mechanisms so that the diagnostics can be reliably controlled. The establishment of the field-induced anodic oxidation cell and the electrochemical reactions giving rise to the nano-oxidation have been depicted schematically in [13]. Briefly, when the AFM tip is brought toward the sample surface in ambient conditions, a water bridge is formed around the tip–sample junction due to the field-induced water condensation and the capillary force of water. AFM tip then acts as a negatively biased cathode with respect to the sample surface, while the adsorbed water meniscus formed between the tip and the sample surface dissociates and acts as electrolyte for the subsequent electrochemical reactions due to the high electric field being established. The chemical reactions and charge transfer processes involved in the anodic oxidation on *p*-GaAs(100) surface have been previously considered as following:

(I) on the *p*-GaAs(100) surface

$$2GaAs + 6H_2O + 12h_{hole}{}^{+} \rightarrow Ga_2O_3 + As_2O_3 + 12H^{+} \quad (1)$$

$$6H_2O + 12h_{hole}{}^{+} \rightarrow 3O_2 \uparrow + 12H^{+} \quad (2)$$

(II) at the AFM tip

$$12H_2O + 12e^{-} \rightarrow 6H_2 \uparrow + 12OH^{-} \quad (3)$$

(III) in water

$$12H^{+} + 12OH^{-} \rightarrow 12H_2O \quad (4)$$

Similar to those discussed in Si [14, 15], within the context of the anodic oxidation concepts, the anionic and cationic transport are important factors in determining the kinetics of oxidation. In this scenario, the driving force is the faradaic current flowing between the tip and sample surface with the aid of the water meniscus. When the faradaic current flows into water bridge, H_2O molecules are decomposed into oxyanions (OH^{-}, O^{-}) and protons (H^{+}). These ions penetrate into the oxide layer because of the electric field (in the order of 10^8 V/cm) [4], leading to the formation and subsequent growth of Ga(As)O_x on the GaAs surface. The directional penetration of the hydroxyl ions could also play a prominent role in enhancing the aspect ratio of protruded oxide structures.

Micro-Auger Analysis

To investigate the chemical composition of the anodized structures, AES analysis was conducted on an anodized area of 10 × 10 μm^2 with oxide thickness being about 5–6 nm. The Auger spectra taken from the as-grown and modified areas are displayed in Fig. 1. It can be seen that both spectra have emission peaks of Ga-*LMM* at $\sim$1065 eV and As-*LMM* at $\sim$1225 eV. From the emission peak of O-*KLL* Auger electrons shown in Fig. 1b, the

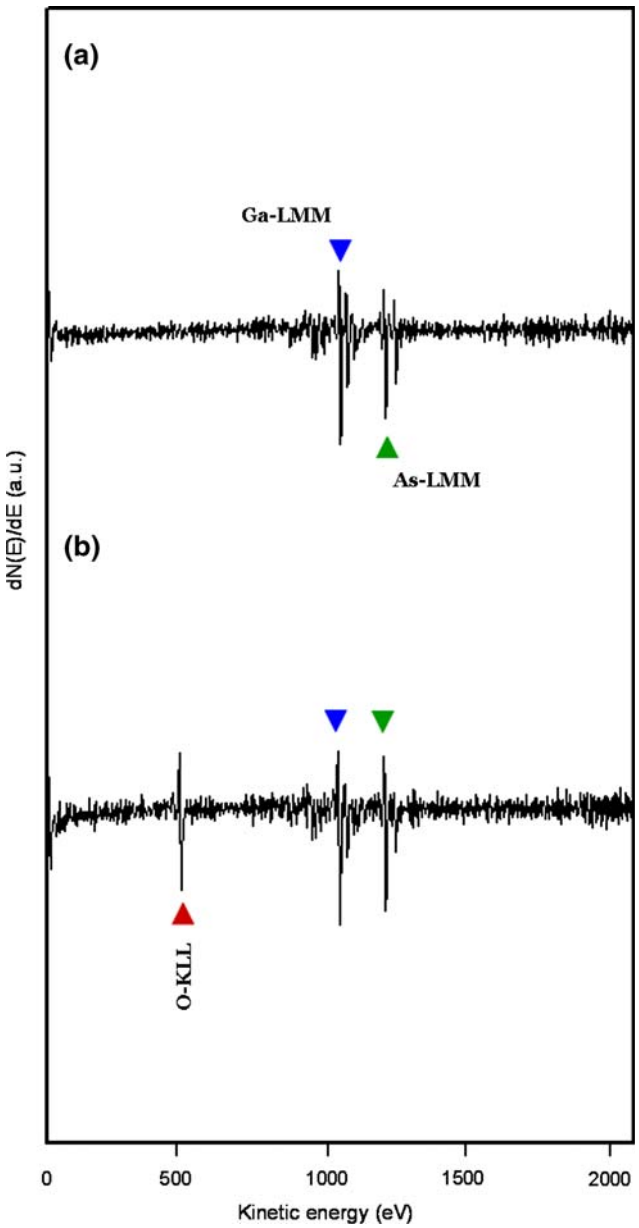

Fig. 1 AES spectra of (**a**) the as-grown and (**b**) the anodized oxide areas on *p*-GaAs(100) surface

obtained kinetic energy of the electrons is ~512 eV. Meanwhile, the magnitude of O-*KLL* is much enhanced on the anodized region as compared to that of the as-grown region, suggesting that the higher oxygen content in GaAs resulted from AFM nanooxidation may have led to the formation of anodized GaAs. AES results also support the suggestion of the previous study [16]. In that the heavily C-doped GaAs film can be converted to oxides by local oxidation process—the mobile oxyanions drift toward the anodized sample in response to the local electrical field beneath an AFM tip and react with *p*-GaAs(100) surface at the oxides/GaAs interface. In addition, X-ray photoelectron spectroscopy (XPS) is also a powerful technique for analyzing surface chemistry and composition. The chemical analysis of AFM tip-induced n^+-GaAs(100) oxides had also revealed that the main constituents are Ga_2O_3 and As_2O_3 as determined by means of the scanning microprobe XPS measurements [17]. Therefore, both AES and XPS analyses have shown, at least qualitatively, that the products are GaAs-derived oxides.

Kinetics of AFM Anodic Oxidation on *p*-GaAs(100) Surface

In Fig. 2a, the height of the oxide nanodots as a function of the anodized time obtained by using the CNT-attached probe and the conventional one are displayed for comparison. It is evident that the height of the protruded point oxides increases concurrently with the pulse duration in both cases, albeit with slightly different slopes, indicating that the oxide growth occurs primarily along the direction (perpendicular to the surface) of the electric field. Notably, the results are similar to those presented in [15], wherein the AFM anodic oxidation has been demonstrated with varying static voltages and pulses of various durations.

The kinetic characteristics of AFM anodic oxidation by the CNT-attached and the conventional probes are further analyzed and discussed below. As is evident from Fig. 2a, with the same time duration, the height of oxide nanodots produced by CNT-attached probe is higher than those obtained by the conventional one. The oxides height for both the CNT-attached and conventional probes, each with an anodized voltage of 8 V, was estimated to be ~6.6 and ~5.1 nm, respectively. Note that, in the estimation, the electrochemical process is assumed to be solid-state diffusion limited. To give a more quantitative account of the growth kinetics, in Fig. 2b, the growth rate of oxide nanodots is plotted as a function of electric field strength. The initial growth rate of oxide nanodots induced by the CNT-attached probe is ~300 nm/s, which is about 15 times larger than that obtained from the conventional one. Also, it can be clearly seen that the growth rate strongly depends on the electric field strength and, in both cases, the anodic oxidation process is greatly enhanced when the electric field strength is beyond the order of $\sim 2 \times 10^7$ V cm^{-1}. In our previous study [13], it has been shown that the growth rate not only is a function of electric field strength but also depends on the applied anodized voltage.

Avouris et al. [14] proposed that the growth kinetics can be described as $dh/dt \propto \exp(-h/l_c)$, where h is the oxide thickness at time t and l_c is a characteristic decay length depending on the anodized voltage. Figure 2c shows the relationships between the growth rate and the oxide height by two different types of probes at an applied voltage of 8 V.

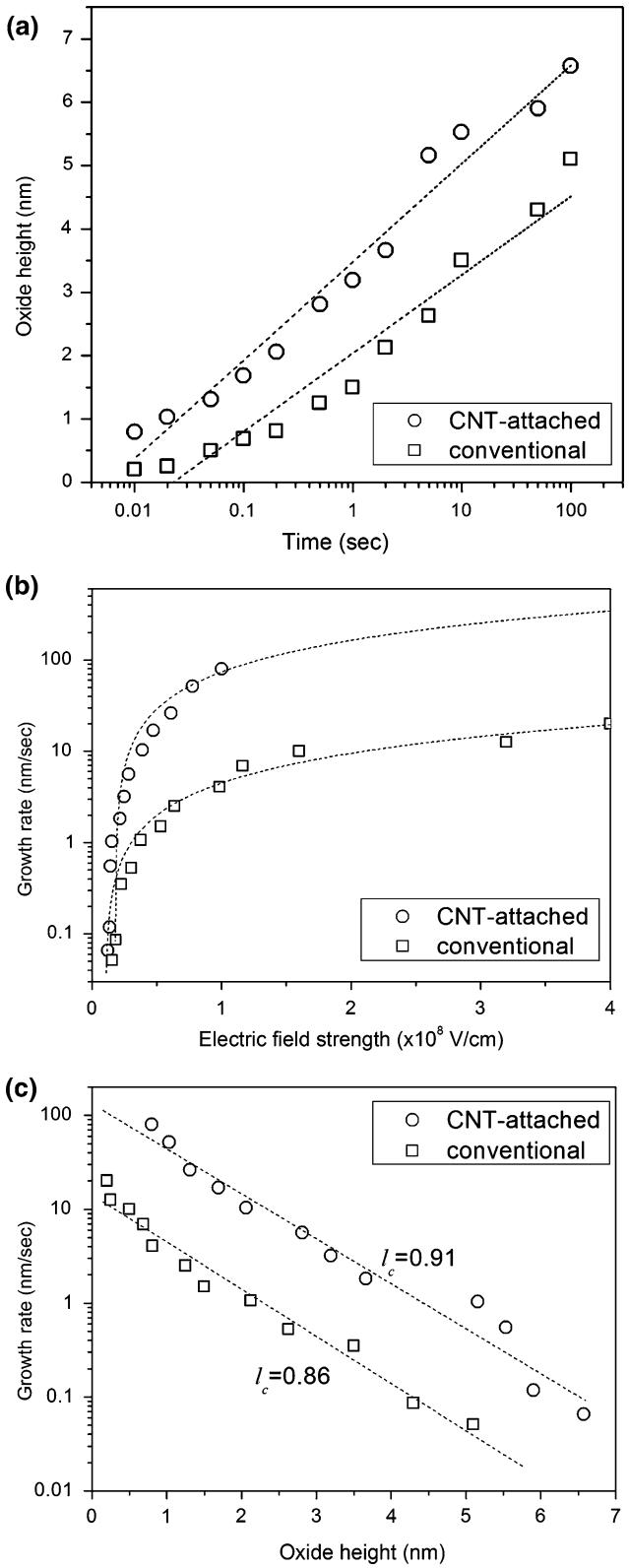

Fig. 2 AFM anodic oxidation by the two different types of probes used in this study: (**a**) Oxide height as a function of the anodization time from 0.01 to 100 s at an anodized voltage of 8 V; (**b**) Relationship of the growth rate and the electric field strength; and (**c**) Oxide height vs. the growth rate

The characteristic decay length, l_c, for CNT-attached and conventional probes are estimated to be 0.91 and 0.86 nm, respectively. Taking into account for the self-limiting mechanisms of AFM tip-induced anodic oxidation, Stiévenard et al. [15] proposed that a greater height of oxide protrusion corresponds to a weaker electrical field strength, which limits the growth of the oxide nanostructures.

According to the above-mentioned results, the growth rate of the oxide nanodots is governed via the ionic transportation promoted by the electric field strength. The growth of the oxides is therefore fast in the initial stage of the anodic oxidation process while there is a rapid build-up of space charge taking place simultaneously. The applied anodized voltage extends the electric field strength, assisting the oxidation mechanisms until the growth is limited by diffusion. It is evident that the simple Cabrera–Mott model [18] of field-induced oxidation is inadequate to account for the observed kinetics shown here. The possible reasons giving rise to the discrepancies between the kinetics of AFM nanooxidation and the Cabrera–Mott field model could be due to: (i) the space charge build-up within the oxide nanodots [19], and (ii) the mechanical stress created and accumulated within the oxide nanodots because of the large volume mismatch between the sample and the oxides [20].

Effect of Pulsed Voltages

Next, we discuss the influence of applying a modulated voltage on the AFM anodic oxidation. The AC square waveform used in the present study is illustrated in Fig. 3a, which consists of a series of pulses where T_{ox} and T_{res} are denoted as the oxidation time and the rest time; V_{ox} and V_{res} are the applied voltages during T_{ox} and T_{res}, respectively. We refer $1/(T_{ox} + T_{res})$ as the frequency of the waveform. The total oxidation time equals to T_{ox} multiply the number of pulses. The oxide nanodots grown by the two different types of probes under AC and DC conditions are illustrated in Fig. 3b for comparison. The results show that, in both cases, the height of the oxides increases by a factor of $\sim$1.1. Similar tendency of enhancement in the height of oxide structures under AC conductions was observed in the previous study [21]. In addition, it can be seen that, with the same conditions, the oxide nanodots grown by using the CNT-attached probe are still much higher. The reasons can be interpreted as given below.

The electrochemical oxidation process is mainly due to the source of hydrogenous species. After a long period of anodization time, the neutralization reaction of OH^- and H^+ becomes more important due to the increasing proton concentration. As a result, less OH^- ions reach the GaAs/$Ga(As)O_x$ interface and the growth rate of the oxide

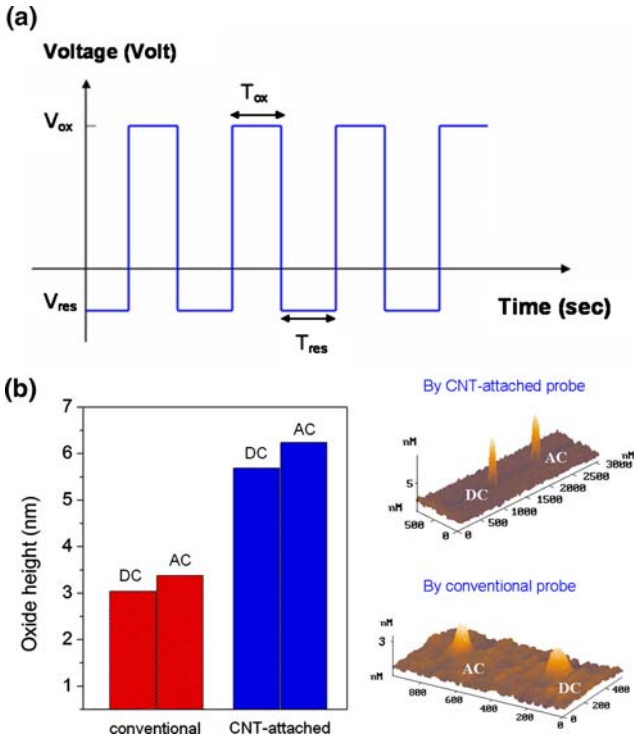

Fig. 3 (**a**) Voltage waveform applied to the GaAs surface with respect to the AFM probe when performing an oxidation under AC conditions: T_{ox} is the time as the oxidation is being performed (the voltage applied to the sample is V_{ox}), and T_{res} is the rest time (the voltage applied is V_{res}); (**b**) the comparison of the oxide height and AFM images of oxide dots by the two different types of AFM tip under DC and AC conditions, right (DC voltage of 8 V and total time = 30 s) and left (AC voltage, $T_{ox} = T_{res} = 50$ ms, $V_{ox} = 8$ V, $V_{res} = -8$ V and total time = 60 s), at the relative humidity of 55%

decreases accordingly. Meanwhile, the lateral diffusion of OH^- at the water/oxide interface becomes more pronounced, leading to the increase of the oxide width. The phenomena of the lateral diffusion can be suppressed, however, by applying an AC voltage with a sequence of negative and positive voltages. In the period of rest time T_{res}, H^+ ions would be taken away from the GaAs/Ga(As)O_x interface and the transport of OH^- ions would be interrupted. It has been demonstrated that a negative voltage V_{res} cannot produce any observable oxide nanodots on the sample surface. Until the next voltage pulse is activated at V_{ox}, the directional transport of OH^- will be re-started and the vertical growth of the oxide nanodot continues. Hence, a shaper structure can be obtained under AC conditions at the central part of the dot where the electric field strength is supposed to be higher.

Table 1 summarizes the oxide nanodots fabricated by the AFM anodic oxidation with the CNT-attached and conventional probes operated at DC and AC conditions. The fact that much higher oxide nanodots are obtained by using the CNT-attached probe may be due to the smaller apex of CNT-attached probe. The smaller probe apex results in the narrower water bridge and more centralized electric field, which, in turn, enhanced the AFM nanooxidation process. Finally, we note that the doping condition of the substrate may also play a role in the nanooxidation process. Teuschler et al. [22] reported that the *p*-type Si(111):H has the higher oxide height and growth rate than that of *n*-type at a particular applied voltage. Thus, in addition to the geometric shape of the AFM probe and the applied voltage scheme presented here, operation conditions, such as the relative humidity and substrate doping, can also be practiced to manipulate the oxide nanodots with desired requirements.

Conclusion

In conclusion, we have presented the results and the associated mechanisms of fabricating oxide nanodots on *p*-GaAs(100) surface by AFM tip-induced lithography with the conventional and CNT-attached probes. In this particular electrochemical reaction, the composition analysis by micro-Auger revealed that the selectively oxidized GaAs area was turned into Ga(As)O_x. The results also indicate

Table 1 Characteristics of AFM anodic oxidation-fabricated oxide nanodots in the present work with comparisons to the results previously reported on the GaAs surface

Probe type	Substrate	Oxide height (nm)	Voltage type	Relative humidity (%)	AFM mode
Conventional Pt-coated Si probe	*p*-GaAs	~6.3	DC	70	NC [23]
	p-GaAs	~5.2	DC	55	NC [#]
	n^+-GaAs	~4.1	DC	40–50	C [24]
	n^+-GaAs	~5	AC	40–50	C [24]
	p-GaAs	~3.4	AC	55	NC [#]
CNT-attached probe	*p*-GaAs	~5.6	DC	55	NC [#]
	p-GaAs	~6.4	AC	55	NC [#]

C: Contact mode; NC: Noncontact mode

[#]: The present work

that the localized anodic oxidation process is significantly enhanced as the electric field strength is beyond $\sim 2 \times 10^7$ V cm^{-1}. The effective electric field, nevertheless, is weakened by the increasing height of the oxide protrusions, which, in turn, limits further growth of the oxide protrusions. Finally, it was demonstrated that the application of AC-voltage scheme can significantly enhance the aspect ratio of the oxide nanodots. The current results, therefore, suggest that the AFM nanolithography with CNT-attached probe could result in much smaller oxide nanostructures, which is of great benefit to the fabrication of integrated nanometer-sized devices.

Acknowledgments This work was partially supported by the National Science Council of Taiwan and I-Shou University, under Grants No. NSC97-2218-E-214-003 and ISU97-07-01-04.

References

1. J.A. Dagata, Science **270**, 1625 (1995). doi:10.1126/science.270.5242.1625
2. T. Vijaykumar, G.U. Kulkarni, Solid State Commun. **142**, 89 (2007). doi:10.1016/j.ssc.2007.01.027
3. V. Bouchiat, M. Faucher, C. Thirion, W. Wernsdorfer, T. Fournier, B. Pannetier, Appl. Phys. Lett. **79**, 123 (2001). doi:10.1063/1.1382626
4. K. Matsumoto, Proc. IEEE **85**, 612 (1997). doi:10.1109/5.573745
5. U.F. Keyser, H.W. Schumacher, U. Zeitler, R.J. Haug, K. Eberl, Phys. Status Solidi **224**, 681 (2001). doi:10.1002/(SICI)1521-3951(200104)224:3<681::AID-PSSB681>3.0.CO;2-D
6. U.F. Keyser, M. Paesler, U. Zeitler, R.J. Huang, K. Eberl, Physica E **13**, 1155 (2002). doi:10.1016/S1386-9477(02)00325-9
7. M.M.J. Treacy, T.W. Ebbesen, J.M. Gibson, Nature **381**, 678 (2002). doi:10.1038/381678a0
8. J.H. Hafner, C.L. Cheung, A.T. Woolley, C.M. Lieber, Prog. Biophys. Mol. Biol. **77**, 73 (2001). doi:10.1016/S0079-6107(01)00011-6
9. E.W. Wong, P.E. Sheehan, C.M. Lieber, Science **277**, 1971 (1997). doi:10.1126/science.277.5334.1971
10. H.J. Dai, N. Franklin, J. Han, Appl. Phys. Lett. **73**, 1508 (1998). doi:10.1063/1.122188
11. A. Okazaki, T. Kishida, S. Akita, H. Nishijima, Y. Nakayama, Jpn. J. Appl. Phys. **39**, 7067 (2000). doi:10.1143/JJAP.39.7067
12. S. Iijima, Nature **354**, 56 (1991). doi:10.1038/354056a0
13. H. Bloeß, G. Staikov, J.W. Schultze, Electrochim. Acta **47**, 335 (2001). doi:10.1016/S0013-4686(01)00581-3
14. P. Avouris, T. Hertel, R. Martel, Appl. Phys. Lett. **71**, 285 (1997). doi:10.1063/1.119521
15. D. Stiévenard, P.A. Fontaine, E. Dubois, Appl. Phys. Lett. **70**, 3272 (1997). doi:10.1063/1.118425
16. J.I. Shirakashi, K. Matsumoto, M. Konagai, Appl. Phys. A **66**, S1083 (1998). doi:10.1007/s003390051302
17. Y. Okada, Y. Iuchi, M. Kawabe, J.S. Harris Jr., J. Appl. Phys. **88**, 1136 (2000). doi:10.1063/1.373788
18. N. Cabrera, N.F. Mott, Rep. Prog. Phys. **12**, 163 (1949). doi:10.1088/0034-4885/12/1/308
19. J.A. Dagata, T. Inoue, J. Itoh, K. Matsumoto, H. Yokoyama, J. Appl. Phys. **84**, 6891 (1998). doi:10.1063/1.368986
20. Y. Okada, S. Amano, M. Kawabe, J.S. Harris Jr., J. Appl. Phys. **83**, 7998 (1998). doi:10.1063/1.367891
21. M. Calleja, J. Anguita, R. García, K. Birkelund, F. Pérez-Murano, J.A. Dagata, Nanotechnology **10**, 34 (1999). doi:10.1088/0957-4484/10/1/008
22. T. Teuschler, K. Mahr, S. Miyazaki, M. Hundhausen, L. Ley, Appl. Phys. Lett. **67**, 3144 (1995). doi:10.1063/1.114861
23. S.R. Jian, T.H. Fang, D.S. Chuu, J. Phys. D: Appl. Phys. (Berl) **38**, 2424 (2005)
24. Y. Okada, Y. Iuchi, M. Kawabe, J. Appl. Phys. **87**, 8754 (2000). doi:10.1063/1.373606